Acta Materialia 246 (2023) 118726

Contents lists available at ScienceDirect

Acta Materialia

journal homepage: www.elsevier.com/locate/actamat

Uniaxial stress increases layer stacking disorder in calcium silicate hydrates with low calcium content

David W. Gardner [a], Jiaqi Li [b], Martin Kunz [c], Wei-Chih Liao [d], Chenhui Zhu [c], Carlo Carraro [a], Paulo J.M. Monteiro [b], Roya Maboudian [a,*]

[a] Department of Chemical and Biomolecular Engineering, University of California Berkeley, 201 Gilman Hall, Berkeley, CA 94720, United States
[b] Department of Civil and Environmental Engineering, University of California Berkeley, Berkeley, CA 94720, United States
[c] Advanced Light Source, Lawrence Berkeley Laboratory, Berkeley, CA 94720, United States
[d] Department of Chemistry, University of California Berkeley, Berkeley, CA 94720 United States

ARTICLE INFO

Keywords:
X-ray diffraction
Creep
Crystal plasticity
Cement
Preferred orientation

ABSTRACT

The long-term stress response of concrete is controlled by the intergrain and intragrain interactions of calcium-silicate-hydrates (C-S-H), nanocrystalline forms of tobermorites. To investigate both types of interactions, we examined the deviatoric stress response of 11 Å tobermorite powder with X-ray diffraction, finding that its layer stacking (i.e., sliding) disorder significantly increases.

A similar experiment was performed on nanocrystalline C-S-H powders before and after applying a 360 MPa uniaxial stress. Layer stacking disorder (in the form of intragrain deformation) increases when there is low water content and when the basal spacing is large. We also find that grains with a smaller thickness-to-diameter aspect ratio are first to develop preferred orientation (in the form of intergrain sliding), facilitated by gel water. These findings show that intragrain deformations in C-S-H can occur at relatively low stresses and provide insights into the creep mechanism of C-S-H.

1. Introduction

1.1. Creep in cement

The long-term response to deviatoric stress through creep in concrete controls the ultimate deformation of the material. Creep in concrete is controlled by the cement matrix, whose main binding phase is calcium (alumino)silicate hydrate. C-(A-)S-H has a lamellar structure (Fig. 1), which is a defective, nanocrystalline form of tobermorite [1], and has structural similarities to the sheet silicates in clays [2,3]. There are two important types of water in C-(A-)S-H: interlayer water (visible in Fig. 1) and gel water. Interlayer water is strongly bound and is considered part of the crystal structure, whereas gel water exists between the grains in the pore structure.

Understanding the mechanism of creep is critical as materials scientists and engineers begin to add supplementary cementitious materials to the blend [5,6], whose effects on the creep compliance are poorly known, mainly relying on semiempirical models. Models for creep of the cement matrix at the nanoscale are often proposed in connection with nanoindentation experiments [7–12]. In these experiments, a C-S-H powder is pressed into a compact, and then a nanoindentation tip is pressed into the compact.

One model of cement matrix creep is the pore-filling model of Vandamme and Ulm [13], which assumes that creep is proportional to void fraction, with rigid grains sliding past each other. The sliding is now thought to take place over a layer of gel water (also called extragranular water), which is considered separately from the interlayer water. This was demonstrated computationally by Morshedifard et al. [14] and experimentally by Suwanmaneechot et al. [11] Both found that creep compliance is highly correlated with gel water, although the dependence was only valid for gel water thickness ~5 Å or greater (this corresponds to relative humidity above ~30%).

1.2. Preferred orientation and creep in cement

An alternate method to study creep is to measure the extent of preferred orientation under a deviatoric stress [14]. The comparison is not perfect, since creep is a time-dependent process, and the methods

* Corresponding author.
E-mail address: maboudia@berkeley.edu (R. Maboudian).

https://doi.org/10.1016/j.actamat.2023.118726
Received 2 June 2022; Received in revised form 18 January 2023; Accepted 22 January 2023
Available online 24 January 2023

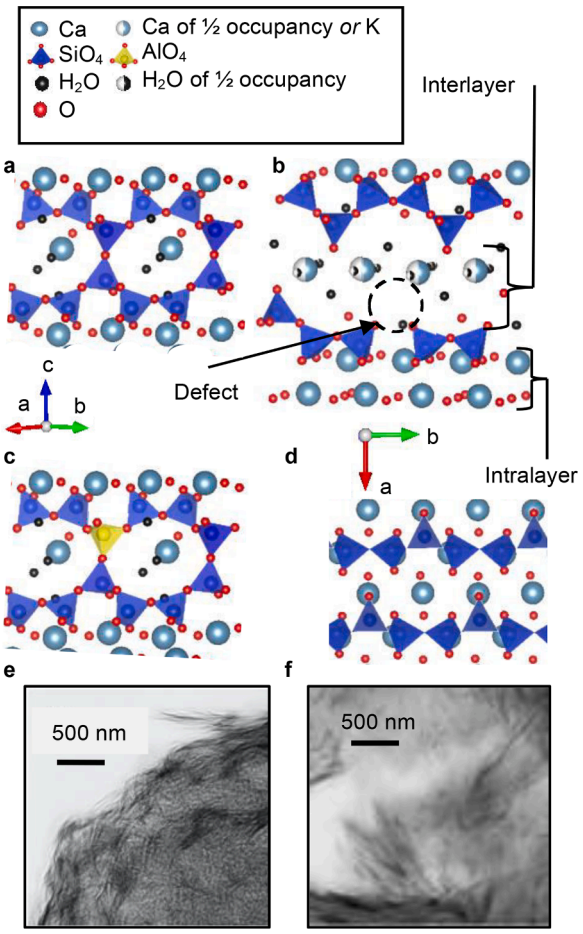

Fig. 1. Crystal structures of (a) cross-linked structure of normal 11 Å tobermorite, (b) non-cross-linked structure of C-S-H and C-K-S-H, (c) Cross-linked structure of C-A-S-H. (d) *ab* plane of C-(X-)S-H. Ptychographic images from Ref. [4] of (e) C-S-H with Ca/Si = 1.0 and (f) C-A-S-H with Ca/Si = 1.0, Al/Si = 0.1.

described below are not strictly measured across time. The basis is that creep in layered materials can occur by mutually sliding planes shearing against each other, as in clays, and C-(A-)S-H has been shown to orient its basal plane towards a deviatoric stress at deviatoric stress as low as 12 MPa [15,16]. Clays and C-(A-)S-H are made up of hydrated inorganic sheets, and their stress response has been studied and analyzed using microplane models [17]. An important clarification is that this paper will primarily focus on C-S-H powders that are pressed to compacts rather than studying a concrete block that is stressed over time. Pressed compacts are the typical sample form for nanoindentation experiments.

Preferred orientation can develop by an *inter*grain mechanism, where rigid grains slide against each other. In the intergrain mechanism, the sliding must be perpendicular to the *c*-axis of the grains because of the grain shape [18] and in accordance with experiments showing *c*-axis alignment with deviatoric stresses [15]. Preferred orientation can also develop by an *intra*grain mechanism, with the same constraint that the most active sliding vectors are perpendicular to the *c*-axis [19].

We have previously shown that intergrain deformations occur in C-S-H under deviatoric stresses of 100's MPa using small-angle X-ray scattering and deviatoric-stress Raman spectroscopy, but there was no connection between structure and extent of reorientation [20]. Other recent experiments with C-S-H with Ca/Si = 1.47 and basal spacing of 9.8 Å show that grain yielding takes place at deviatoric stresses ~ 100 MPa though the characterization was limited to X-ray diffraction [16].

1.3. Multiscale characterization approach

In this paper, we investigate the connection between preferred orientation, intergrain sliding, and intragrain deformations towards understanding how C-S-H water content and morphology affect development of preferred orientation. We study highly crystalline normal 11 Å tobermorite and four C-S-H samples that vary in calcium, alkali, and aluminum content. We refer to them collectively as C-(X-)S-H, where X = K, Al, or nothing.

These samples are compacted and the changes to their crystal structures are studied with X-ray diffraction. First, a diamond anvil cell is used with the tobermorite sample, because the stress field felt by the tobermorite sample can be measured. Later, a pellet press is used with the C-S-H samples, because a more realistic stress can be used. X-ray diffraction is used to study changes in layer stacking disorder within a sample, using the relative peak ratios of a sample's basal peak and *hk* peaks. Because of the full 360° detector geometry we can also acquire information about the variations in average microstress and average coherent scattering length with grain orientation. Changes in average size are difficult to clearly show in an XRD pattern, so small-angle X-ray scattering is used to more clearly show if there are changes in grain size.

Gel water is known to be extremely important to C-S-H grains sliding. We use two characterization methods to probe the thickness of gel water: thermogravimetric analysis and 1H NMR T2 relaxometry.

2. Experimental

2.1. C-(X-)S-H synthesis

C- S-H samples were synthesized at an initial bulk Ca-to-Si molar ratio (Ca/Si) of 1.0 and 1.2 and C-A-S-H samples with initial bulk Ca/Si of 1.0 and initial bulk Al-to-Si molar ratios (Al/Si) of 0.05. Stoichiometric amounts of $CaO{\cdot}Al_2O_3$, fumed SiO_2 (Aerosil 200, Evonik), and CaO (from calcined $CaCO_3$) were mixed with deionized water at a water-to-solid mass ratio of 45 in a N_2-filled glove box. The C-S-H was cured for 56 days at 50 °C. The cross-linked C-A-S-H sample with Al/Si of 0.05 was cured for 182 days at 80 °C. The C-K-S-H sample was prepared at Ca/Si of 1.0 in 0.5 M KOH solution at a liquid-to-solid mass ratio of 45 in a N_2-filled glove box. The C-K-S-H sample was cured for 56 days at 50 °C. After vacuum filtration, the wet samples were freeze-dried for 7 days. Freeze drying removes some gel water from the C-S-H powders compared to non-dried powders, possibly leading to a metastable powder with less gel water than would be present in a non-freeze-dried powders [21–23].

The dry powders were equilibrated in N_2-filled desiccators at 30% relative humidity, then sealed in vacuum bags until analysis. For more details on synthesis methods, see Refs. [24,25]. We intentionally avoided high Ca/Si samples, even though these are more relevant to widely used cements, because high Ca/Si samples' crystallinity is not as good for X-ray diffraction characterization and are more easily contaminated by atmospheric CO_2.

2.2. Compact pressing

C-(X-)S-H powder was loaded using a dry pellet pressing die (diameter 3.175 mm, MTI). A vertical force was applied to exert a maximum uniaxial stress of 360 MPa on the sample with a hydraulic press; the maximum loading was held for 300s. The C-(X-)S-H was tested as a pressed compact rather than in a diamond anvil cell because it is easier to apply the desired uniaxial stress in a press and collect the sample for other characterization.

Then the die was unloaded. The final products after compaction were compacts with ~1 mm thickness. The compacts were tested 24 h after compaction. Two compacts were made for each sample. Compacts were tested first by X-ray diffraction, then stored in vacuum to minimize carbonation. Subsequent small-angle X-ray scattering experiments were

done within one week of pressing.

2.3. Compact and Diamond Anvil Cell (DAC) X-ray diffraction

The XRD experiments were conducted at the superbend beamline 12.2.2 [26] of the Advanced Light Source (ALS) at the Lawrence Berkeley National Laboratory. The incident X-ray beam energy was 25 keV (wavelength ~0.4959 Å), and the beam size was ~15 μm with the convergence of the focused beam of ~0.18°. A MAR345 image plate with 100 μm square pixels was used as a detector for collecting 2D diffraction images. The sample-to-detector distance was ~330 mm in all experiments and was calibrated using a CeO_2 standard. These measurements were conducted at room temperature. The exposure time for each compact measurement was 600 s, and the exposure time in a DAC was 1800 s. For ambient pressure measurement, the powder samples were loaded into glass capillaries.

As shown in Fig. 3, to probe as many crystal orientations relative to the compression direction as possible, a radial geometry DAC was chosen where the incident beam was perpendicular to the symmetry axis of the DAC, which was also the principal loading direction. The gasket was made by laser drilling a 100 μm diameter hole into an 80 μm thick Be gasket, which was then placed on the diamond. The assembly was covered in Kapton tape as a safety precaution against Be dust.

The sample was loosely packed into the gasket hole. The load was applied by slowly tightening the load screws of the DAC. A thin piece of Pt was placed between one diamond anvil culet and the sample powder. Since no pressure medium was used, the stress in the sample was initially zero, which began to build up as soon as the inter-particle porosity was essentially eliminated by the increasing compressive load. The diffraction peaks of Pt were analyzed to calibrate the pressure and deviatoric stresses in the sample chamber [27].

Considering the symmetry of the experimental setup, the macroscopic elastic stress tensor has the following non-zero components in the sample coordinate system:

$s_{11} = s_{22} = P - S$, $s_{33} = P + 2S$, where s_{11} is the transverse stress, s_{33} is the axial stress, P is pure hydrostatic component (pressure), and S is the deviatoric component of the stress [28,29]. Here, positive values are used for compression.

We assume that the same stresses, i.e. not only the axial stress but also the transverse stresses, are shared between the powder and the Pt grains. This Reuss approximation (namely, equal stress in every grain) is often considered in geophysics research using high-pressure DAC in radial geometry [19]. High deviatoric stresses can develop in a DAC, so it is relevant to check that the Pt grains have not yielded. Dorfman et al. reported that the yielding of platinum strongly depends on the loading conditions [30] and the grain size, and it can happen at differential stress (S/3 by our definition) values below 1 GPa. In the present experiment, the values of the deviatoric stress are less than 300 MPa, and there is no evidence of intensity redistribution along Pt Debye rings, which would have indicated the onset of the plastic deformation; the rings were also close to circular throughout. Therefore, our estimations of deviatoric stresses in C-(A-)S-H under pressure should not be significantly biased.

2.5. Rietveld refinement

The input phase for the all C-A-S-H samples is the monoclinic normal 11 Å tobermorite (Merlino) of space group B11m [31]. The raw 2D diffraction image (Fig. 3) was sliced into segments spanning an azimuthal angle of 10°. MAUD was used to calculate the crystal *c* parameters. More details are provided in the supplementary material.

2.6. Azimuthal X-ray diffraction analysis

To determine the order parameter of the compact, we measured the diffracted intensity for the (002) peak at azimuthal intervals of 10°. To determine the intensity, a Gaussian distribution of I(q) was fit for each azimuthal slice of the 2-D XRD pattern after subtracting a polynomial background. This was used to determine the order parameter <S2> [32,33], where <S2> = 0 indicates isotropy and <S2> = 1 indicates perfect alignment. Order parameter is used throughout to facilitate comparison to simulations of hard-disk-like ensembles.

MAUD was not capable of calculating a distribution of crystal sizes and strains by azimuthal slice as quickly as could be performed in a numerical package like the SciPy package. Rietveld analysis of peak widths for individual azimuthal slices was performed with the following assumptions:

$$B(\eta,\ hkl) = B_{microstrain}(\eta,\ hkl) + B_{CSL}(\eta,\ hkl) + B_{pellet} \tag{1a}$$

$$B_{pellet} = 0.01 * 0.5 * 2\theta(hkl) \tag{1b}$$

$$B_{microstrain}(\eta,\ hkl) = 4 *\ \varepsilon(\eta, hkl) * \frac{\sin(0.5 * 2\theta(hkl))}{\cos(0.5 * 2\theta(hkl))} \tag{1c}$$

$$\varepsilon(\eta, hkl) = E_{hkl} * Stress(\eta) \tag{1d}$$

$$Stress(\eta) = Uniaxial\ stress * (0.3 + 0.7 * \sin(\eta)) \tag{1e}$$

$$CSL_{hkl} = \frac{\lambda}{\cos(0.5 *\ Two - Theta(hkl))} * B_{CSL}(\eta,\ hkl) \tag{1f}$$

where B(*h,hkl*) is the full width half maximum of a peak fit to a Gaussian in a particular azimuth slice, *h* is the azimuth slice (0° representing the right-hand-side or 3-o'clock position, positive for counterclockwise from 0), *hkl* are the scattering vector indices for the peak, $B_{microstrain}$ is the microstrain contribution to the width, B_{CSL} is the finite length contribution to the width, B_{pellet} is the pellet thickness contribution to the width (with the factor of 0.01 derived from the 3-mm-thick pellet placed 300 mm away from the detector), 2θ (hkl) is the peak center, ε_{hkl} is the strain of the axis, E_{hkl} is the compressibility of the axis derived from literature (in practice, 290 GPa for the (020), (220) peak for all samples, 160 GPa for C-S-H Ca/Si = 1.0, 200 GPa for C-S-H Ca/Si = 1.2, 240 GPa for C-A-S-H, 200 GPa for C-K-S-H), Stress(*h*) is the stress at that azimuth (a sinusoidal dependence is assumed and looks to be vindicated by the total width as a function of azimuth; the factor of 0.3 is the Poisson ratio for tobermorite-like-structures [34]), l is the X-ray wavelength (0.4959 Å), and CSL is the coherent scattering domain size in Å. Instrument contributions to peak widths from the synchrotron beam and detector are negligible compared to the observed peak widths and the instrumentation widths are constant along the azimuth.

Each detector image was broken into 90 azimuthal slices. The peak width of the (002) peak was determined by fitting one Gaussian peak to the right-hand side of the (002) peak. (Interferences from low-angle scattering and the beamstop led to artifacts in the fits if the entire peak was used). The peak width of the (020), (220) peak was determined by fitting two Gaussians in the range q = 2.0 to 2.3 $Å^{-1}$ for C-A-S-H and C-S-H, and three Gaussians for C-K-S-H to account for the main calcite peak.

2.7. Thermogravimetric analysis of powders and compacts

To determine gel water content, powder samples and compacted samples were loaded in a thermogravimetric analysis (TGA) instrument, a Shimadzu TGA-50 analyzer. The heating rate was 5 °C/minute in nitrogen. Powders were allowed to equalize with humidity (50% relative humidity at 25 °C) for 24h before analysis.

The gel water content was determined by estimating the weight fraction of water in the sample that can be assigned to interlayer water by estimating the interlayer water content based on basal spacing [35]. Interlayer water content was estimated from basal spacing as opposed to integration of multiple peaks on a d%/dT plot because of nonuniform interlayer water binding energy during the experiment [36] and the severe temperature gradient that exists in a pellet during the experiment

(Fig. S1). Other notes on the TGA methods are provided in the supplementary material.

2.8. Frequency filtered 1H NMR relaxometry

Powders were allowed to equalize with ambient humidity (50% relative humidity at 25 °C) for 24h before analysis. NMR data were acquired using a 11.7 T Bruker magnet and a Bruker Advance I spectrometer that operates at the frequency of 500.23 MHz for 1H NMR. The chemical shifts were externally referenced to the downfield resonance of adamantane at 38.38 ppm relative to trimethylsilane. Experiments were performed using a Bruker 4 mm double resonance (1H/X) cross polarization magic angle spinning probe. Powders were loaded into a 4 mm (outer diameter) zirconia rotor. Samples were spun with N_2 gas at the magic angle spinning rate of 12 kHz. The 1H pulse powers were set to 85 kHz. A Carr-Purcell-Meiboom-Gill (CPMG) echo sequence [37] was used to modulate the 1H signal with the T2 relaxation before the data was recorded for the free induction decay. Each experiment was time averaged 32 times with a recycle delay of 5 s and an acquisition time of 50 milliseconds. The echo delay for the CPMG sequence was set to two rotor cycles (TE=0.167 ms), and the experiments were repeated with increasing number of echo trains to give a total decay time of 0.17, 0.25, 0.33, 0.42, 0.50, 0.58, 0.67, 0.83, 1.2, 2.5, 3.33, 5.0, 6.7, 8.3, 11.7, and 15.0 ms. Raw NMR data is uploaded in Fig. S2. The zero ms decay time experiment was not used due to interference from a broad interlayer water peak.

The T2 decay curve for the gel water resonance was fit to a mono-exponential T2 decay (Fig. S3). Typical R^2 values for this fit are between 0.92 and 0.98 indicating an excellent fit, and the points are evenly scattered around the trendline. More details of NMR methodology are provided in the supplementary material.

2.9. Small angle X-ray scattering

Small-angle X-ray scattering (SAXS) were carried out at beamline 7.3.3 at the Advanced Light Source at Lawrence Berkeley National Lab [38] with a beam energy E = 10 keV, a bandwidth DE/E = 1% and a beam size about 300 x 700 mm^2 with a q-range between 0.004 and 0.4 $Å^{-1}$. Small-angle scattering has been shown to provide information about the size, geometry, and density of C-S-H particles [4,39–42].

Pressed compacts were loaded into 1 mm diameter capillaries by lightly breaking up the compact by hand in a mortar and pestle and collecting the pieces into a capillary. Scattering patterns were recorded on a two-dimensional Pilatus 2M detector (Dectris), which has a pixel size of 172 mm. The exposure time used was less than 5 s. The X-ray beam position on the detector and the sample to detector distance were calibrated using the standard silver behenate. The two-dimensional data were calibrated and azimuthally averaged into one-dimensional intensity, I, vs. scattering vector, q, using Igor Pro Nika package [43]. The 1D data were analyzed by numerically integrating the full form factor for a disk [44], assuming a discretized normal distribution of thicknesses (i.e. contribution only from integer multiples of the basal spacing) and with a constant aspect ratio for each sample (Eqs. (1a)–(1e)) [45]:

$$I(q) = I_0 \sum_{i=1}^{\infty.} F_i^2(q) * S(q) * \text{Weight}(i \text{ basal spacings}) \tag{1a}$$

$$\text{Weight}(i \text{ basal spacings}) = \exp\left(\frac{(i-\mu)^2}{2\sigma^2}\right) \tag{1b}$$

$$F^2{}_i(q) = \int_0^{\pi/2} \text{abs}\left(\frac{\sin(qT_i\cos\phi)}{qT_i\cos\phi} * \frac{2J_1(qR_i\sin(\phi))}{qR_i\sin(\phi)}\right)^2 \sin(\phi)d\phi \tag{1c}$$

$$T_i = 0.5 * i * \text{basal spacing} \tag{1d}$$

$$\text{Aspect ratio} = \frac{T_i}{2R_i} = \text{constant} \tag{1e}$$

where $I(q)$ is the intensity at the scattering vector q, I_0 is an intensity factor, $S(q)$ is the static structure factor, $F_i(q)$ is the single particle form factor, i is an index for the number of basal spacings in the grain, μ is the mean number of basal spacings, σ is the standard deviation of the distribution, T_i is half the sample thickness, R_i is the average particle radius (related to the thickness by the aspect ratio), and ϕ is the angle between the normal to the disk plane and the scattering vector q. The fitting procedure was taken after Ref. [45] with the primary goal of extracting the average grain thickness. In fact, the q-range we used to target the thickness was not sufficient to extract the diameter, so only the thickness and the distribution deviation will be reported.

In just one case, the powder 11 Å Tobermorite sample, the low-angle resolution was not sufficient to resolve the thickness, indicating a thickness greater than 30 nm. In all other cases the reciprocal of the first radius of gyration was greater than the lowest magnitude scattering vector [46].

Multiple scattering events in dense samples tend to smooth out small-angle X-ray scattering patterns, and the average power-law dependence of I(q) at a given q is not affected [47]. Using the method and results of Ref. [47], we estimate a scattering power of ~0.1 in the powders and ~ 1 in the compacts. The effect of multiple scattering on our small-angle patterns reduces the influence of the static structure factor but has minimal effect on the influence of the particle form factor. More details on the fitting procedure are given in the supplementary materials.

3. Results and discussion

3.1. Radial diamond anvil cell compaction of crystalline 11 Å normal tobermorite

The ambient 1-D XRD pattern of the normal 11 Å tobermorite in Fig. 4 shows symmetric peaks. (For the full patterns, see Fig. S4.) The results of the Rietveld refinement are given in Table S1. Upon compaction in the diamond anvil cell, the sample's (002) peak shows a strain of 9% at a stress condition of P = 3.9 GPa and S = 0.3 GPa. The order parameter of the (002) peak is <S2> = 0.84. The rings corresponding to the most intense *hk* peaks are not visible on the detector image, although they are very weakly present in the azimuthally integrated pattern. Deloading the sample (P <1 GPa and S ~ 0 GPa, the gray "unload" trace with <S2> = 0.67) shows that the (002) peak has not changed its position from ambient, although the peak is a bit wider. The main *hk* peaks' spectral intensity is now completely gone.

This is inciting question of this paper: What happened to the *hk* peaks in our tobermorite sample under uniaxial stress, and might a similar mechanism be taking place in C-S-H under uniaxial stress? Layer stacking defects are necessary to explain the findings, as these have significant effects on *hk* peak intensity, whereas increases in microstrain and decreases in coherent scattering length are insufficient (Fig. S5). Given (i) the layered structure of tobermorites, (ii) the prevalence of layered stacking defects in layered structures [48], (iii) our prior Raman spectroscopy findings that C-(A-)S-H can slip in its *ab* plane at S < 0.3 GPa [20], and (iv) the inadequacy of simpler microstructural changes to account for the peak ratio change, an increase in layer stacking disorder is the most plausible explanation [49]. Following this experiment, we set out to investigate if similar disorder is induced in C-S-H under uniaxial stress.

3.2. X-ray diffraction of C-(X)-S-H samples

3.2.1. Changes to diffraction patterns upon compaction

Fig. 5a, b show the azimuthally averaged pattern of the samples after compaction in a pellet press at 360 MPa uniaxial stress. Finite element

Table 1
Basal peak parameters as calculated by MAUD and grain thickness as measured by SAXS. Values in parentheses represent two standard deviations of the fit parameter combined with the measurement standard deviation from two samples. There was not sufficient material of the C-S-H Ca/Si = 1.0 compact to study by SAXS.

Sample		c (Å)	<S2>	SAXS Grain Thickness (Å)
C-A-S-H	Powder	22.9 (<0.1)	0	100 (0.8)
	Compact	22.8 (<0.1)	0.37 (<0.1)	63 (0.5)
C-S-H	Powder	20.7 (<0.1)	0	83 (4.8)
Ca/Si = 1. 2	Compact	20.5 (<0.1)	0.47 (<0.1)	59 (3.5)
C-S-H	Powder	23.2 (<0.1)	0	66 (2.5)
Ca/Si = 1.0	Compact	23.1 (<0.1)	0.47 (<0.1)	–
C-K-S-H	Powder	21.7 (<0.1)	0	158 (2.8)
	Compact	21.6 (<0.1)	0.26 (<0.1)	133 (2.3)

analyses of plastically deforming grains in compaction show that the maximum shear stresses felt are ~10% of the uniaxial stress, so in our case, the estimated shear stress on the grains is roughly 40 MPa [50]. Applying an effective Poisson ratio to the powder of 0.3 [51,52] leads to a transverse stress (σ_T) equal to ~150 MPa and a deviatoric stress of 60 MPa while forming the pellet. This estimate of the deviatoric stress S is an upper bound because the effective Poisson ratio for powders is greater than the value for a solid material.

The basal-peak summary of Rietveld refinement is given in Table 1 (Full results in Table S2). X-ray diffraction patterns and their fits are given in Figs. S6–S9, and plots of basal peak intensity vs. azimuth is given in Fig. S10. After compaction all peaks have similar changes in the XRD pattern. In the following discussion right- and left-shifts are considered for the patterns plotted against the scattering vector, q. All peaks right-shift, especially the (002) peak.

Basal peak widths increase upon compaction. To determine if the width increase is entirely due to residual stress or if grain thickness also decreases, we used small-angle X-ray scattering to estimate the grain thickness, assuming that the grains are roughly disk-shaped (full SAXS patterns provided in Figs. S11–S17, fit parameters Table S3). We are assuming that the grain thickness is essentially parallel to the crystal <002> [18].

The SAXS patterns on a log-log plot show the intensity has a -2.5 power dependence at low q and a -4 power dependence at high q. Simply put, the transition wavevector between the two regimes is proportional to the average grain thickness, assuming a disk-like morphology [47]. In the compacts' SAXS patterns, the transition is at higher q than the respective powder's patterns, indicating that the grain thickness decreases. Other features of the SAXS patterns are beyond the scope of this paper.

The *hk* peaks get wider after compaction. Some of the extra peak width can be attributed to the thickness of the compact compared to the capillary, but based on the geometry of the compact, ~3 mm diameter and ~330 mm from the detector, there is only an extra 1% of the q vector magnitude. For the (020) peak, this adds ~0.02 $Å^{-1}$. Another factor is microstrain. This variable is constrained by the compliance tensor and the stresses of the experiment. Only reductions in coherent scattering domain size (i.e. fracture) can compensate the increased width.

Another phenomenon that could affect the X-ray diffraction patterns of compacted disks is out-of-plane deformations caused by the compaction, especially bending along *a* or *b*. These deformations would have a significant effect on the *hk* peak widths (Fig. 5c–f), but we see essentially no increase, indicating that this out-of-plane deformation is not dominant.

3.2.2. *Changes to diffraction patterns by azimuth and 'phase separation'*

In the C-A-S-H and C-K-S-H sample, the (020), (220) peak width of all azimuthal slices of the compact is indistinguishable from the width of this peak in the powder sample. The expected azimuthal dependence of the peak width from the packing is not even present, meaning that most of the stress is dissipated.

In the two C-S-H samples, the (020), (220) peak of the compact is wider than the powder peak, but only for azimuthal slices between 60° and 120°. For other azimuthal slices, the peak width of the compact is actually *less* than the peak width of the powder, which can only be possible if there is segregation by grain thickness.

Fig. 6 shows the average aspect ratio plotted versus the orientation of the grains' c-axis. In the C-S-H samples there is a clear dip in the aspect ratio for grains in the ordered phase aligned with the previously applied stress.

Simulations of rigid disks with a distribution of aspect ratios, defined as thickness divided by diameter, show that the compaction leads to the development of two distinct phases: an 'isotropic' (<S2> = 0) phase and a 'nematic' phase (<S2> > 0). When there are two phases present in a heterogeneous mixture, the nematic phase will always have a lower average aspect ratio than the isotropic phase [28,29,53–55].

By analogy with simulations, we can conclude that the C-S-H samples relied on intergrain interactions to develop their preferred orientation. However, the C-A-S-H and C-K-S-H samples show no dip in aspect ratio with c-axis orientation, so intergrain sliding is unlikely to have been the dominant mechanism. More research is needed with high-spatial-resolution tools (e.g., TEM [56]) to conclude definitively that spatially distinct 'nematic' phases develop in C-S-H under stress.

3.2.3. *Controlling for the effect of preferred orientation on hk peak intensity*

The layer stacking disorder can be indirectly quantified by comparing the actual intensity of the first *hk* peak (the (020), (220) peak) with the predicted intensity if no layer stacking defects were generated (Fig. 7). C-S-H have layer stacking disorder after their synthesis [57,58], and this section discusses an increase in their layer stacking disorder following compaction.

If the grains are rigid while developing preferred orientation, then

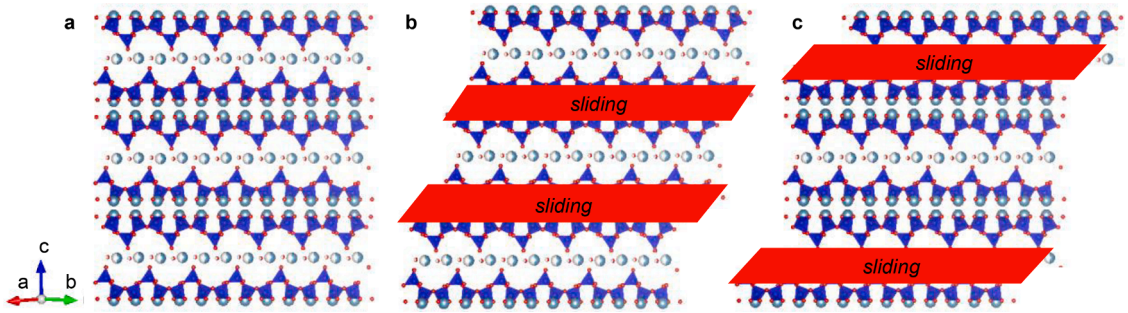

Fig. 2. Sliding disorders in 14 Å tobermorite. Key to atom symbols is as in Fig. 1. Some interlayer atoms are removed for clarity. (a) Crystal structure. (b) Layer stacking disorder with sliding defect along *b* in the CaO_7 *intra*layer. (c) Layer stacking disorder with sliding defect along *b* in the *inter*layer. Depicted displacement is arbitrary and does not correspond to any experimental result.

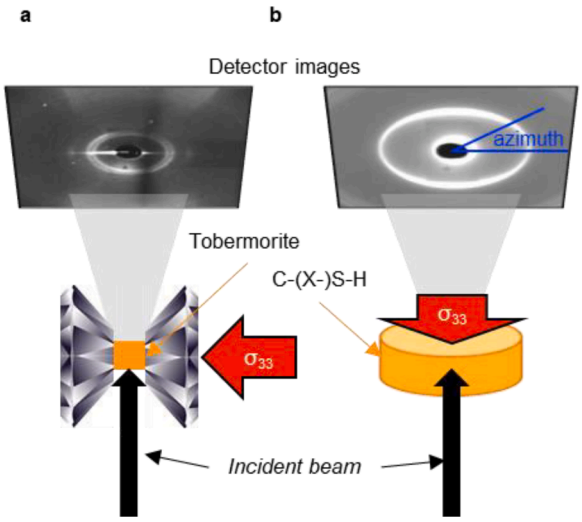

Fig. 3. Geometry of scattering experiments for (a) diamond anvil cell experiment and (b) compact experiments. Note that the stress is applied along 0 and 180° for the diamond experiments but 90 and 270° for compacts.

points along the black trace of Fig. 7 will be observed. However, if layer stacking disorder increases during compaction, the *hk* peaks become relatively less intense, and points will lie closer to the red trace of Fig. 7. The black trace is valid for crystalline and disordered layered materials because the points are normalized to an isotropic case; the red trace represents an *increase* in layer stacking disorder.

The C-S-H sample with Ca/Si = 1.2 lies nearly on the black trace, indicating that it did not develop preferred orientation by means of intragrain sliding (Fig. 2). However, the C-S-H sample with Ca/Si = 1.0 does see some extinction of its *hk* peaks. The Ca/Si = 1.0 sample has a larger basal spacing than the higher Ca/Si C-S-H sample (11.5 Å vs ~10 Å), so it is reasonable to expect more sliding along the Ca/Si = 1.0 interlayer, since the energetic barrier to slide decreases with spacing between faces [59]. The higher Ca/Si result is supported by a separate experiment in a diamond anvil cell. C-S-H with Ca/Si = 1.47 and basal spacing ~ 9.8 Å achieved a preferred orientation primarily by an intergrain mechanism at deviatoric stresses < 100 MPa [16].

The C-K-S-H and C-A-S-H samples both show an increase in layer stacking disorder (intragrain deformations). We have previously studied the evolution in bond strain with stress in the C-A-S-H sample, albeit at higher stresses, finding that it likely slips on the seven-fold-coordinate Ca intralayer, as its interlayer is crossed by strong silicate chains [35]. It is known that Al in C-A-S-H can occupy several electronic states (essentially as an interlayer component or in the silicate chain [60,61]) and depending on the relative fraction of each state the Al has different effects. We cannot determine the exact method of the C-K-S-H sample's deformation, but because its interlayer is not cross-linked [24], it is reasonable to assume there is slip on either or both the interlayer or intralayer.

3.3. Water characterization

Gel water is known to lubricate grains sliding against each other

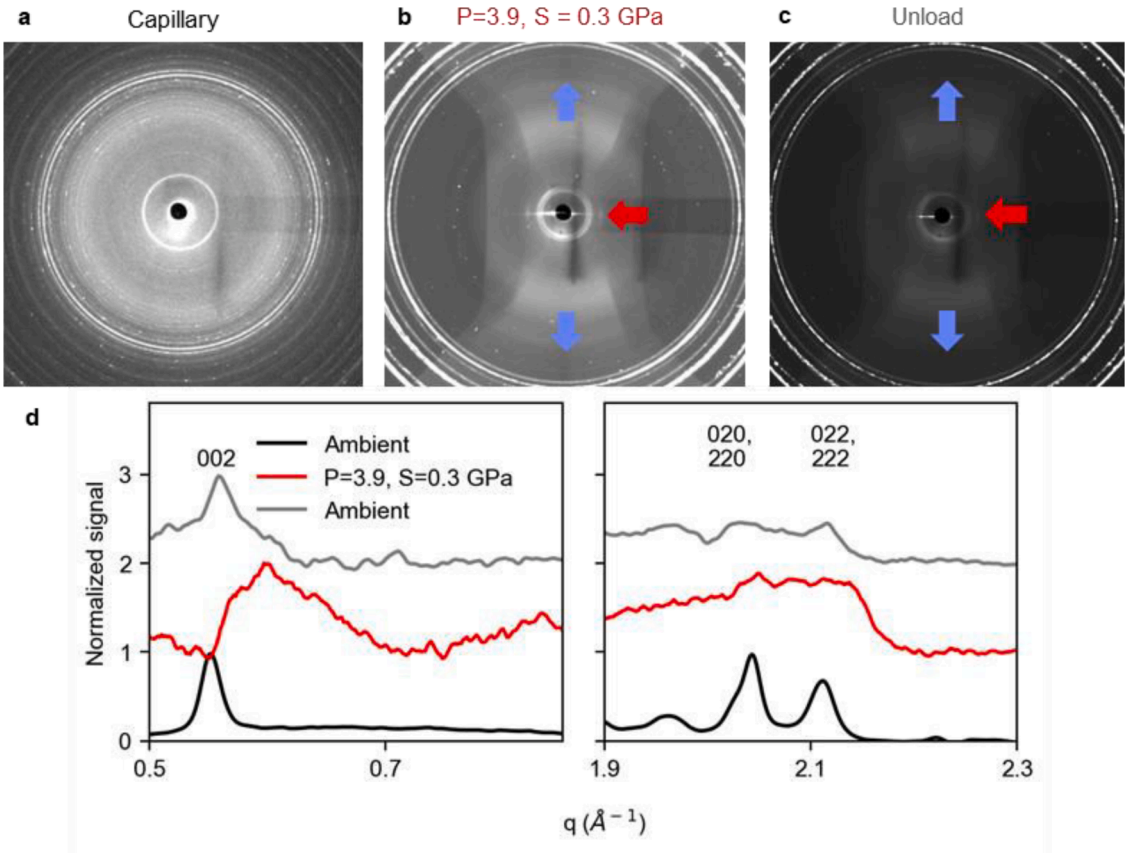

Fig. 4. Compaction of the crystalline 11 Å normal tobermorite in a diamond anvil cell. (a-c) Detector images in capillary, in diamond anvil cell, and after unloading screws. The red arrows correspond to the Debye ring for the (002) peak and the blue arrows point to where the ring for the (020), (220). The (002) peak is aligned with the stress. (d) Azimuthally integrated 1-D XRD pattern in the region of the main peaks after background subtraction. Patterns normalized to the (002) peak intensity. The loss of spectral intensity in *hk* peaks suggests an increase in layer stacking disorder following compaction. (For interpretation of the references to colour in this figure legend, the reader is referred to the web version of this article.)

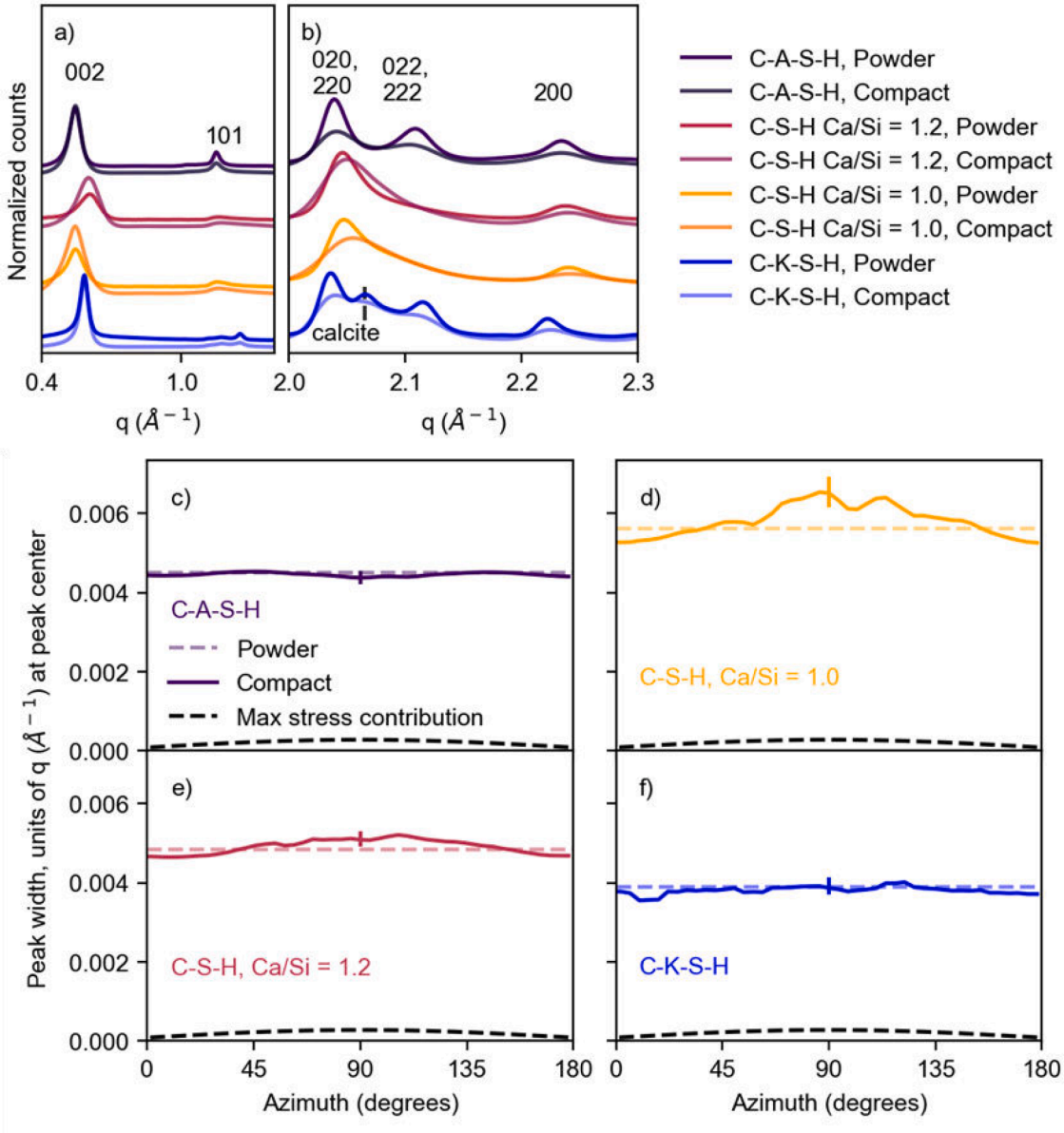

Fig. 5. Azimuthally averaged, intensity-normalized XRD patterns of C-(X-)S-H powders and compacts. Patterns are normalized to the most intense peak. (a) Basal peak. (b) First *hk* peaks. (c-f) FWHM of the (020), (220) peak, given in units of q at the peak's center position. The stress contribution is plotted assuming that there is no stress dissipation after compaction. An azimuth of 90° is parallel to the stress used to prepare the compact. The only contributions to peak width that meaningfully vary along the azimuth are variations in average microstress and in average coherent scattering length.

(inter-grain deformation) to achieve a preferred orientation [11]. We used two techniques to measure the thickness of gel water to support our above findings: TGA and frequency-filtered and 1H NMR T2 relaxometry. Raw TGA plots are given in Fig. S1, and raw 1H NMR plots are given in Figs. S4, S5. Based on the results of Section 3.2, we should expect the intergrain-deforming powders to have more gel water than intragrain-deforming powders. There is almost no difference in gel water content amongst the C-S-H powders, while C-S-H with Al and K tend to decrease the amount of gel water (Fig. 8a). There is a positive relationship between the extent of ordering and the gel water content, supporting the XRD conclusions.

Results from 1H NMR tell a similar story. Powders with larger T2 relaxation constants (where larger relaxation constants indicate thicker gel water films [62–64]) develop more preferred orientation. Powders with thicker water films have lower barriers to intergrain sliding [14]. There is a very strong relationship between T2 relaxation constant for the dominant water and the order parameter that the sample achieves under uniaxial stress (Fig. 8b). We postulate that larger T2 constants correlate with increasing thickness of mobile water which mobile water lubricates grain-grain sliding, as we describe above.

3.4. Interplay between preferred orientation, intergrain deformation, and creep

Fig. 9 shows why the C-A-S-H and C-K-S-H samples deform by intragrain deformations, while the 1.0 Å C-S-H sample does not. The shear stress on a slip system is normalized by the grain's orientation to the stress by a factor of sin(θ)cos(θ) [19], also called the Schmid factor, where θ is the angle between the stress and the sliding vector in the grain. The factor is zero when the sliding is perpendicular to the applied stress (θ = 90°), as is the case for an already oriented compact. The C-A-S-H and C-K-S-H samples cannot deform much by intergrain mechanisms from isotropic for lack of lubricating gel water, so their Schmid factor is large; whereas the 1.2 Ca/Si (~10 Å basal spacing)

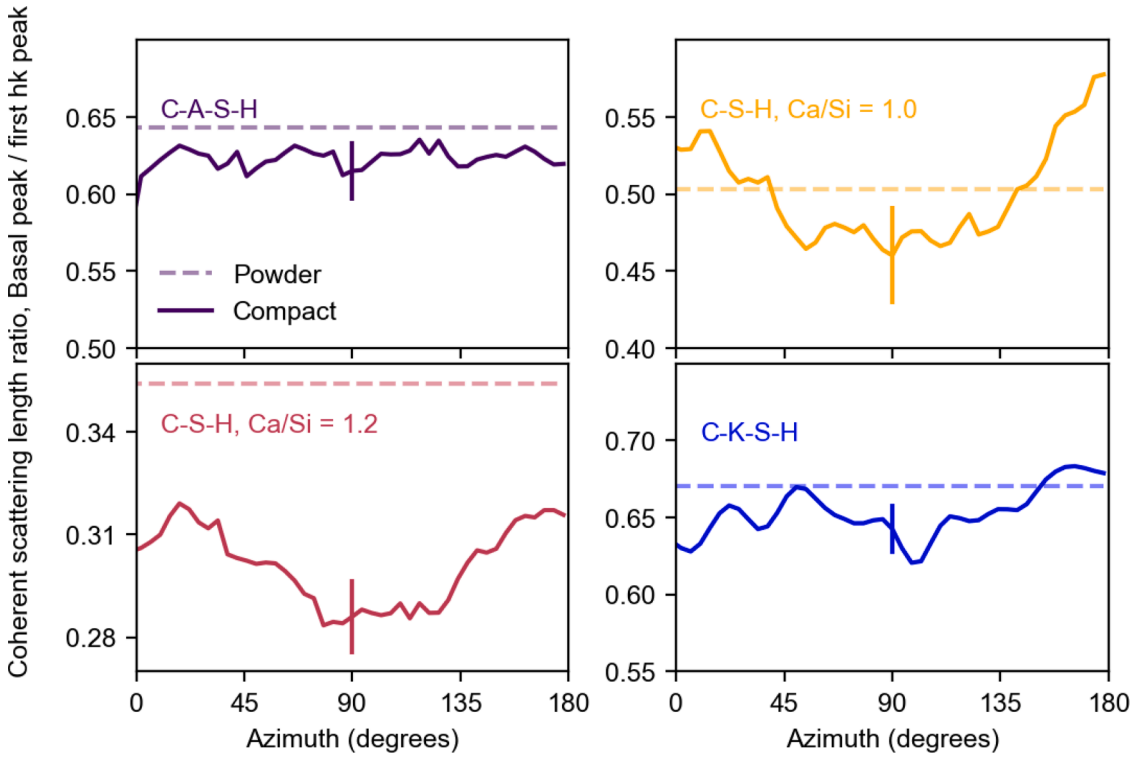

Fig. 6. Aspect ratio, defined as the coherent scattering length of the (002) peak at azimuth angle divided by the coherent scattering length of the (020), (220) peak at +90° azimuth. A grain orientation of 90° means that the c-axis is aligned with the deviatoric stress. Error bars represent two standard errors in each direction from the aspect ratio parameters estimate. Standard error of parameter estimate is nearly constant across the azimuthal range.

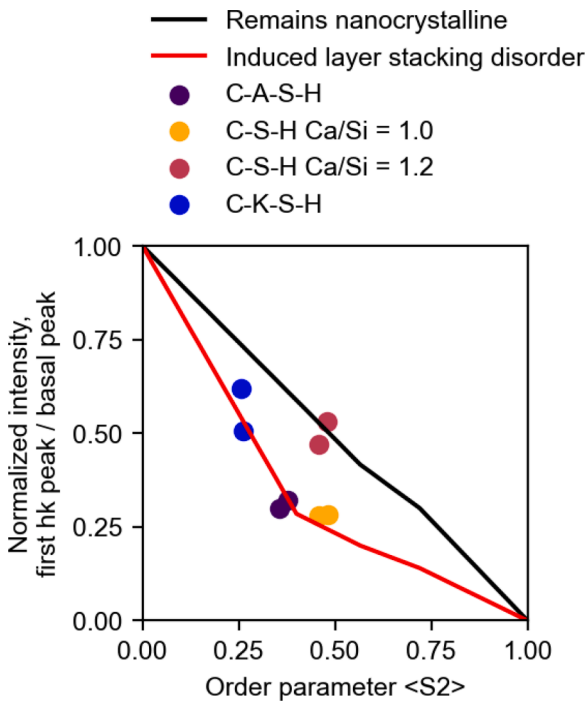

Fig. 7. Peak extinction of the (020), (022) peaks for each sample. The error bars along each axis are <0.01 for each data point.

C-S-H sample *does* develop a preferred orientation by intergrain mechanisms first, so once the porosity is reduced and <S2> ~ 0.5, the Schmid factor is much smaller. The 1.0 Ca/Si (11.5 Å basal spacing) C-S-H sample has a lower threshold to slide by its larger interlayer so its layer stacking disorder increases as it develops preferred orientation. These effects are important to consider in nanoindentation experiments [15,16,65].

4. Conclusions

C-(X)-S-H, the main binding phase in concrete made with Portland cement and arbiter of its creep behavior, responds to deviatoric stress by developing a preferred orientation. Intragrain deformations play a large role when there is little porosity *or* when the basal spacing is large; otherwise intergrain sliding dominates. A larger study is needed to more fully understand how important basal spacing is for intragrain deformations.

Upon compaction, the first *hk* peak decreases in intensity relative to the basal peak *beyond* what would be expected for a given preferred orientation, indicating stress-induced layer stacking disorder. If there is sufficient gel water, then intergrain sliding will favor the lowest aspect ratio grains entering into an ordered phase. In real C-S-H with higher Ca/Si ratio and that is not freeze-dried, this effect is probably even more relevant than our findings suggest.

The most important finding is that simulations assuming rigid grains tend to make proper qualitative predictions [14], but once gel water content is reduced below 5-6% of total mass, layer stacking deformations (sliding/rotating on intralayer or a large interlayer) allow the grains to deform more than would be expected [10]. Future models of cement creep should account for the yielding of C-S-H grains to shear stress.

Declaration of Competing Interest

The authors declare that they have no known competing financial interests or personal relationships that could have appeared to influence the work reported in this paper.

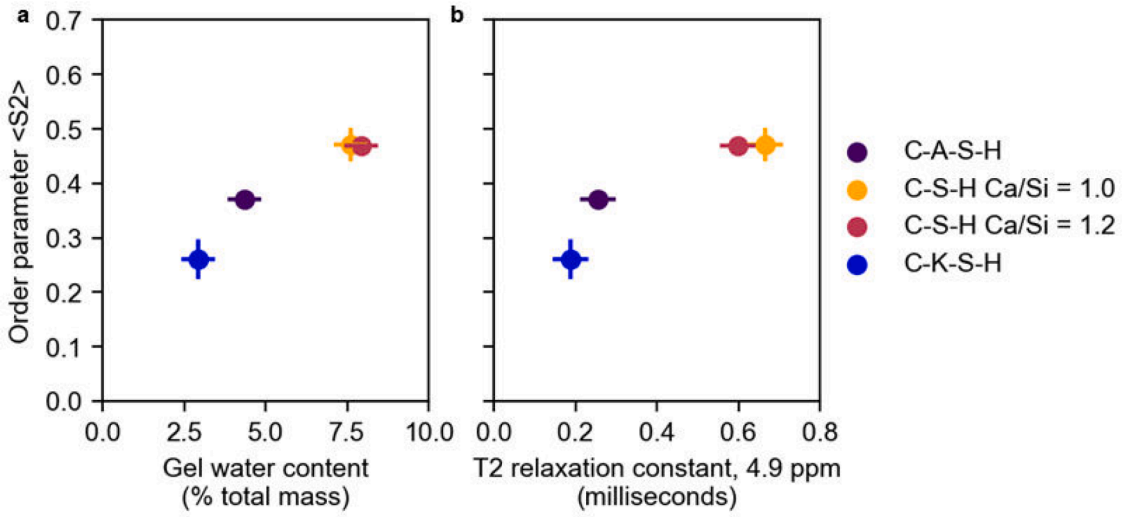

Fig. 8. Relationship between water content and ordering under 300 MPa uniaxial stress. Horizontal axis units are related to the thickness of gel water surrounding a grain. Vertical error bars on both represent two standard deviations of the measurement from two samples. (a) Gel water content by TGA. Horizontal error bars represent two sample standard deviations. (b) Frequency-filtered 1H NMR T2 relaxation data. Horizontal error bars represent two standard deviations of the fit slope.

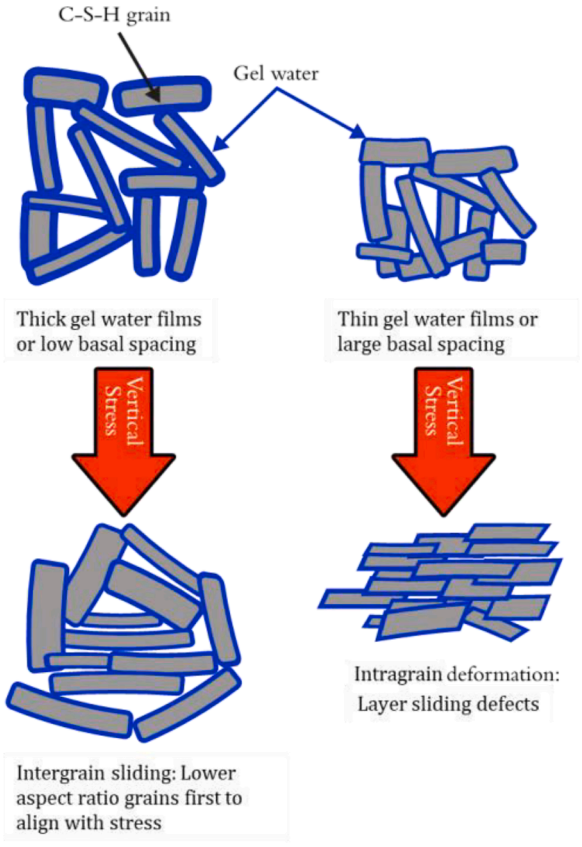

Fig. 9. Compaction mechanism of C-(X-)S-H at a grain level. If there is sufficient water, then intergrain sliding is favored, with low-aspect-ratio grains condensing first. If porosity is low or the basal spacing is large, then layer stacking disorder will increase.

Acknowledgements

The authors thank Barbara Lothenbach for providing the C-(X-)S-H samples synthesized by Rupert J. Myers at EMPA in Zürich, Switzerland, and Jorge Dolado for providing the tobermorite sample synthesized by Valentina Musumeci at the Materials Physics Center in San Sebastián, Spain.

The support of the National Science Foundation under the Division of Materials Research Ceramics Program, DMR-CER, Grant No. 1935604 is gratefully acknowledged. This material is also based upon work partially supported by the U.S. Department of Energy, Office of Science, Office of Workforce Development for Teachers and Scientists, Office of Science Graduate Student Research (SCGSR) program. The SCGSR program is administered by the Oak Ridge Institute for Science and Education (ORISE) for the DOE. ORISE is managed by ORAU under contract number DE-SC0014664. All opinions expressed in this paper are the author's and do not necessarily reflect the policies and views of DOE, ORAU, or ORISE.

The Advanced Light Source is supported by the Director, Office of Science, Office of Basic Energy Sciences, of the U.S. Department of Energy under Contract No. DE-AC02-05CH11231. Beamline 12.2.2 and sample preparation of this research are partially supported by COMPRES, the Consortium for Materials Properties Research in Earth Sciences under NSF Cooperative Agreement EAR 1606856.

Supplementary materials

Supplementary material associated with this article can be found, in the online version, at doi:10.1016/j.actamat.2023.118726.

References

[1] I.G. Richardson, The calcium silicate hydrates, Cem. Concr. Res. 38 (2008) 137–158, https://doi.org/10.1016/j.cemconres.2007.11.005.
[2] R.T. Cygan, J.-J. Liang, A.G. Kalinichev, Molecular models of hydroxide, oxyhydroxide, and clay phases and the development of a general force field, J. Phys. Chem. B. 108 (2004) 1255–1266, https://doi.org/10.1021/jp0363287.
[3] A. Moshiri, D. Stefaniuk, S.K. Smith, A. Morshedifard, D.F. Rodrigues, M.J.A. Qomi, K.J. Krakowiak, Structure and morphology of calcium-silicate-hydrates cross-linked with dipodal organosilanes, Cem. Concr. Res. 133 (2020), 106076, https://doi.org/10.1016/j.cemconres.2020.106076.
[4] J. Li, G. Geng, R. Myers, Y.S. Yu, D. Shapiro, C. Carraro, R. Maboudian, P.J. M. Monteiro, The chemistry and structure of calcium (alumino) silicate hydrate: a study by XANES, ptychographic imaging, and wide- and small-angle scattering, Cem. Concr. Res. 115 (2019) 367, https://doi.org/10.1016/j.cemconres.2018.09.008. –278.
[5] S.A. Miller, A. Horvath, P.J.M. Monteiro, Readily implementable techniques can cut annual CO_2 emissions from the production of concrete by over 20%, Environ. Res. Lett. 11 (2016), 074029 https://doi.org/10.1088/1748-9326/11/7/074029.
[6] B. Lothenbach, K. Scrivener, R.D. Hooton, Supplementary cementitious materials, Cem. Concr. Res. 41 (2011) 1244–1256, https://doi.org/10.1016/j.cemconres.2010.12.001.

[7] M.J. Abdolhosseini Qomi, F.J. Ulm, R.J.M. Pellenq, Physical origins of thermal properties of cement paste, Phys. Rev. Appl. 3 (2015), 064010, https://doi.org/10.1103/PhysRevApplied.3.064010.

[8] E. Masoero, E. Del Gado, R.J.M. Pellenq, F.J. Ulm, S. Yip, Nanostructure and nanomechanics of cement: polydisperse colloidal packing, Phys. Rev. Lett. 109 (2012) 3–6, https://doi.org/10.1103/PhysRevLett.109.155503.

[9] K. Ioannidou, K.J. Krakowiak, M. Bauchy, C.G. Hoover, E. Masoero, S. Yip, F. J. Ulm, P. Levitz, R.J.M. Pellenq, E. Del Gado, Mesoscale texture of cement hydrates, Proc. Natl. Acad. Sci. 113 (2016) 2029–2034, https://doi.org/10.1073/pnas.1520487113.

[10] M. Vandamme, F.J. Ulm, Nanoindentation investigation of creep properties of calcium silicate hydrates, Cem. Concr. Res. 52 (2013) 38–52, https://doi.org/10.1016/j.cemconres.2013.05.006.

[11] P. Suwanmaneechot, A. Aili, I. Maruyama, Creep behavior of C-S-H under different drying relative humidities: interpretation of microindentation tests and sorption measurements by multi-scale analysis, Cem. Concr. Res. 132 (2020), 106036, https://doi.org/10.1016/j.cemconres.2020.106036.

[12] R. Hay, J. Li, K. Celik, Influencing factors on micromechanical properties of calcium (alumino) silicate hydrate C-(A-)S-H under nanoindentation experiment, Cem. Concr. Res. 134 (2020), 106088, https://doi.org/10.1016/j.cemconres.2020.106088.

[13] M. Vandamme, F.J. Ulm, Nanogranular origin of concrete creep, Proc. Natl. Acad. Sci. U. S. A. 106 (2009) 10552–10557, https://doi.org/10.1073/pnas.0901033106.

[14] A. Morshedifard, S. Masoumi, M.J. Abdolhosseini Qomi, Nanoscale origins of creep in calcium silicate hydrates, Nat. Commun. 9 (2018) 1785, https://doi.org/10.1038/s41467-018-04174-z.

[15] G. Geng, R.N. Vasin, J. Li, M.J.A. Qomi, J. Yan, H.R. Wenk, P.J.M. Monteiro, Preferred orientation of calcium aluminosilicate hydrate induced by confined compression, Cem. Concr. Res. 113 (2018) 186–196, https://doi.org/10.1016/j.cemconres.2018.09.002.

[16] J. Li, W. Zhang, Preferred orientation of calcium silicate hydrate and its implication to concrete creep, Compos. Part B Eng. 247 (2022), 110297.

[17] Z.P. Bažant, J.K. Kim, Creep of anisotropic clay: microplane model, J. Geotech. Eng. 112 (1986) 458–475, https://doi.org/10.1061/(ASCE)0733-9410(1986)112, 4(458).

[18] S.M. Mutisya, C.R. Miranda, The surface stability and morphology of tobermorite 11 Å from first principles, Appl. Surf. Sci. 444 (2018) 287–292, https://doi.org/10.1016/j.apsusc.2018.03.002.

[19] H.R. Wenk, P. Van Houtte, Texture and anisotropy, Rep. Prog. Phys. (2004), https://doi.org/10.1088/0034-4885/67/8/R02.

[20] D.W. Gardner, J. Li, M. Kunz, C. Zhu, P. Monteiro, R. Maboudian, C. Carraro, Plastic deformation mechanism of calcium-silicate hydrates determined by deviatoric-stress Raman spectroscopy, Cem. Concr. Res. 146 (2021), 106476.

[21] Q. Zeng, K. Li, T. Fen-Chong, P. Dangla, Water removal by freeze-drying of hardened cement paste, Dry. Technol. 31 (2013) 67–71.

[22] R. Trettin, A. Korpa, he influence of different drying methods on cement paste microstructures as reflected by gas adsorption: comparison between freeze-drying (F-drying), D-drying, P-drying and oven-drying methods, Cem. Concr. Res. 36 (2006) 634–649.

[23] J. Zhang, G.W. Scherer, Comparison of methods for arresting hydrations of cement, Cem. Concr. Res. 41 (2011) 1024–1036.

[24] R.J. Myers, E. L'Hôpital, J.L. Provis, B. Lothenbach, Effect of temperature and aluminium on calcium (alumino)silicate hydrate chemistry under equilibrium conditions, Cem. Concr. Res. 68 (2015) 83–93, https://doi.org/10.1016/j.cemconres.2014.10.015.

[25] R.J. Myers, E. L'Hôpital, J.L. Provis, B. Lothenbach, Composition-solubility-structure relationships in calcium (alkali) aluminosilicate hydrate (C-(N, K-)A-S-H), Dalton. Trans. 44 (2015) 13530–13544, https://doi.org/10.1039/c5dt01124h.

[26] M. Kunz, A.A. MacDowell, W.A. Caldwell, D. Cambie, R.S. Celestre, E.E. Domning, R.M. Duarte, A.E. Gleason, J.M. Glossinger, N. Kelez, D.W. Plate, T. Yu, J.M. Zaug, H.A. Padmore, R. Jeanloz, A.P. Alivisatos, S.M. Clark, A beamline for high-pressure studies at the Advanced Light Source with a superconducting bending magnet as the source, J. Synchrotron. Radiat. 12 (2005) 650–658, https://doi.org/10.1107/S0909049505020959.

[27] E. Menéndez-Proupin, A.K. Singh, Ab initio calculations of elastic properties of compressed Pt, Phys. Rev. B Condens. Matter Mater. Phys. 76 (2007), 054117, https://doi.org/10.1103/PhysRevB.76.054117.

[28] M.A. Bates, Influence of particle shape on the nematic - Isotropic transition of colloidal platelet systems, J. Chem. Phys. 111 (1999) 1732, https://doi.org/10.1063/1.479433.

[29] M. Marechal, A. Cuetos, B. Martínez-Haya, M. Dijkstra, Phase behavior of hard colloidal platelets using free energy calculations, J. Chem. Phys. 134 (2011), 094501, https://doi.org/10.1063/1.3552951.

[30] S.M. Dorfman, S.R. Shieh, T.S. Duffy, Strength and texture of Pt compressed to 63 GPa, J. Appl. Phys. 117 (2015), 065901, https://doi.org/10.1063/1.4907866.

[31] S. Merlino, E. Bonaccorsi, T. Armbruster, The real structure of tobermorite 11Å: normal and anomalous forms, OD character and polytypic modifications, Eur. J. Miner. 13 (2001) 577–590, https://doi.org/10.1127/0935-1221/2001/0013-0577.

[32] P. Davidson, D. Petermann, A.M. Levelut, The measurement of the nematic order parameter by X-ray scattering reconsidered, J. Phys. II. 5 (1995) 113–131, https://doi.org/10.1051/jp2:1995117.

[33] M.T. Sims, L.C. Abbott, R.M. Richardson, J.W. Goodby, J.N. Moore, Considerations in the determination of orientational order parameters from X-ray scattering experiments, Liq. Cryst. 46 (2019) 11–24, https://doi.org/10.1080/02678292.2018.1455227.

[34] R. Shahsavari, M.J. Buehler, R.J.M. Pellenq, F.J. Ulm, First-principles study of elastic constants and interlayer interactions of complex hydrated oxides: case study of tobermorite and jennite, J. Am. Ceram. Soc. 92 (2009) 2323–2330, https://doi.org/10.1111/j.1551-2916.2009.03199.x.

[35] D.W. Gardner, J. Li, S. Masoumi, M.J.A. Qomi, P.J.M. Monteiro, R. Maboudian, C. Carraro, Silicate bond characteristics in calcium-silicate-hydrates determined by high pressure raman spectroscopy, J. Phys. Chem. C 124 (2020) 18335–18345.

[36] C. Roosz, S. Gaboreau, S. Grangeon, D. Prêt, V. Montouillout, N. Maubec, S. Ory, P. Blanc, P. Vieillard, P. Henocq, Distribution of water in synthetic calcium silicate hydrates, Langmuir 32 (2016) 6794–6805, https://doi.org/10.1021/acs.langmuir.6b00878.

[37] S. Meiboom, D. Gill, Modified spin-echo method for measuring nuclear relaxation times, Rev. Sci. Instrum. 29 (1958) 688–691, https://doi.org/10.1063/1.1716296.

[38] A. Hexemer, W. Bras, J. Glossinger, E. Schaible, E. Gann, R. Kirian, A. MacDowell, M. Church, B. Rude, H. Padmore, A SAXS/WAXS/GISAXS beamline with multilayer monochromator, J. Phys. Conf. Ser. 247 (2010), 012007, https://doi.org/10.1088/1742-6596/247/1/012007.

[39] A.J. Allen, J.J. Thomas, H.M. Jennings, Composition and density of nanoscale calcium–silicate–hydrate in cement, Nat. Mater. 6 (2007) 311–316.

[40] S. Brisard, C.A. Davy, L. Michot, D. Troadec, P. Levitz, Mesoscale pore structure of a high-performance concrete by coupling focused ion beam/scanning electron microscopy and small angle X-ray scattering, J. Am. Ceram. Soc. 102 (2019) 2905–2923, https://doi.org/10.1111/jace.16059.

[41] W.S. Chiang, E. Fratini, F. Ridi, S.H. Lim, Y.Q. Yeh, P. Baglioni, S.M. Choi, U. S. Jeng, S.H. Chen, Microstructural changes of globules in calcium-silicate-hydrate gels with and without additives determined by small-angle neutron and X-ray scattering, J. Colloid Interface Sci. 398 (2013) 67–73, https://doi.org/10.1016/j.jcis.2013.01.065.

[42] S. Bae, R. Taylor, D. Shapiro, P. Denes, J. Joseph, R. Celestre, S. Marchesini, H. Padmore, T. Tyliszczak, T. Warwick, D. Kilcoyne, P. Levitz, P.J.M Monteiro, Soft X-ray ptychographic imaging and morphological quantification of calcium silicate hydrates (C-S-H), J. Am. Ceram. Soc. (2015), https://doi.org/10.1111/jace.13808.

[43] J. Ilavsky, Nika: software for two-dimensional data reduction, J. Appl. Crystallogr. 45 (2012) 324–328, https://doi.org/10.1107/S0021889812004037.

[44] M. Kroon, W.L. Vos, G.H. Wegdam, Structure and formation of a gel of colloidal disks, Phys. Rev. E Stat. Phys. Plasmas Fluids, Relat. Interdiscip. Top. 19 (1998) 887–894, https://doi.org/10.1103/PhysRevE.57.1962.

[45] R.A. Vaia, W. Liu, H. Koerner, Analysis of small-angle scattering of suspensions of organically modified montmorillonite: implications to phase behavior of polymer nanocomposites, J. Polym. Sci. Part B Polym. Phys. 41 (2003) 3214–3236, https://doi.org/10.1002/polb.10698.

[46] B. Hammouda, A new Guinier-Porod model, J. Appl. Crystallogr. 43 (2010) 719, https://doi.org/10.1107/S0021889810015773.

[47] F.V. Jensen, J.G. Barker, Effects of multiple scattering encountered for various small-angle scattering model functions, J. Appl. Crystallogr. 51 (2018) 1455–1466.

[48] L.A.G. Aylmore, J.P. Quirk, Domain or turbostratic structure of clays, Nature 187 (1960) 1046–1048, https://doi.org/10.1038/1871046a0.

[49] A. Leonardi, D.L. Bish, Understanding powder X-ray diffraction profiles from layered minerals: the case of kaolinite nanocrystals, Inorg. Chem. 59 (2020) 5357–5367, https://doi.org/10.1021/acs.inorgchem.9b03464.

[50] C.Y. Wu, O.M. Ruddy, A.C. Bentham, B.C. Hancock, S.M. Best, J.A. Elliott, Modelling the mechanical behaviour of pharmaceutical powders during compaction, Powder Technol. 152 (2005) 107–117, https://doi.org/10.1016/j.powtec.2005.01.010.

[51] D. Tunega, A. Zaoui, Understanding of bonding and mechanical characteristics of cementitious mineral tobermorite from first principles, J. Comput. Chem. 32 (2011) 306–314, https://doi.org/10.1002/jcc.21622.

[52] F. Puertas, M. Palacios, H. Manzano, J.S. Dolado, A. Rico, J. Rodríguez, A model for the C-A-S-H gel formed in alkali-activated slag cements, J. Eur. Ceram. Soc. 31 (2011) 2043–2056, https://doi.org/10.1016/j.jeurceramsoc.2011.04.036.

[53] M.A. Bates, D. Frenkel, Nematic-isotropic transition in polydisperse systems of infinitely thin hard platelets, J. Chem. Phys. 110 (1999) 6553, https://doi.org/10.1063/1.478558.

[54] A.F. Mejia, Y.W. Chang, R. Ng, M. Shuai, M.S. Mannan, Z. Cheng, Aspect ratio and polydispersity dependence of isotropic-nematic transition in discotic suspensions, Phys. Rev. E Stat. Nonlinear Soft Matter Phys. 85 (2012), 061708, https://doi.org/10.1103/PhysRevE.85.061708.

[55] R.P.S. Fartaria, N. Javid, J. Sefcik, M.B. Sweatman, Simulation of scattering and phase behavior around the isotropic-nematic transition of discotic particles, J. Colloid Interface Sci. 377 (2012) 94–104, https://doi.org/10.1016/j.jcis.2012.03.046.

[56] P. Viseshchitra, P. Ercius, P.J.M. Monteiro, M. Scott, D. Ushizima, J. Li, K. Xu, H. R. Wenk, 3D Nanotomography of calcium silicate hydrates by transmission electron microscopy, J. Am. Ceram. Soc. 104 (2020) 1852–1862.

[57] S. Grangeon, F. Claret, C. Lerouge, F. Warmont, T. Sato, S. Anraku, C. Numako, Y. Linard, B. Lanson, On the nature of structural disorder in calcium silicate hydrates with a calcium/silicon ratio similar to tobermorite, Cem. Concr. Res. 52 (2013) 31–37, https://doi.org/10.1016/j.cemconres.2013.05.007.

[58] X. Cong, R.J. Kirkpartick, 29Si MAS NMR study of the structure of calcium silicate hydrate, Adv. Cem. Based Mater. 3 (1996) 144–156.

[59] S. Masoumi, H. Valipour, M.J. Abdolhosseini Qomi, Interparticle interactions in colloidal systems: toward a comprehensive mesoscale model, ACS Appl. Mater. Interfaces 9 (2017) 27338–27349, https://doi.org/10.1021/acsami.7b08465.

[60] J. Li, W. Zhang, P. Sanz-Camacho, M. Duttine, D. Gardner, C. Carraro, R. Maboudian, T. Huthwelker, The nanomechanical properties of non-crosslinked calcium aluminosilicate hydrate: the influences of tetrahedral Al and curing age, Cem. Concr. Res. 159 (2022), 106900.
[61] M.J.A. Qomi, F.J. Ulm, R.J.M. Pellenq, Evidence on the dual nature of aluminum in the calcium-silicate-hydrates based on atomistic simulations, J. Am. Ceram. Soc. 95 (2012) 1128–1137.
[62] I. Maruyama, T. Ohkubo, T. Haji, R. Kurihara, Dynamic microstructural evolution of hardened cement paste during first drying monitored by 1H NMR relaxometry, Cem. Concr. Res. 122 (2019) 107–117, https://doi.org/10.1016/j.cemconres.2019.04.017.
[63] A.C.A. Muller, K.L. Scrivener, A.M. Gajewicz, P.J. McDonald, Densification of C-S-H measured by 1H NMR relaxometry, J. Phys. Chem. C 117 (2013) 403–412, https://doi.org/10.1021/jp3102964.
[64] A.M. Gajewicz, E. Gartner, K. Kang, P.J. McDonald, V. Yermakou, A 1H NMR relaxometry investigation of gel-pore drying shrinkage in cement pastes, Cem. Concr. Res. 86 (2016) 12–19, https://doi.org/10.1016/j.cemconres.2016.04.013.
[65] J. Li, W. Zhang, P.J.M. Monteiro, Preferred orientation of calcium aluminosilicate hydrate compacts: implications for creep and indentation, Cem. Concr. Res. 143 (2021), 106371, https://doi.org/10.1016/j.cemconres.2021.106371.